Electrochimica Acta 260 (2018) 150–156

Contents lists available at ScienceDirect

Electrochimica Acta

journal homepage: www.elsevier.com/locate/electacta

Enhanced photoelectrochemical activity in the heterostructure of vertically aligned few-layer MoS_2 flakes on ZnO

Tran Nam Trung, Dong-Bum Seo, Nguyen Duc Quang, Dojin Kim, Eui-Tae Kim*

Department of Materials Science & Engineering, Chungnam National University, Daejeon 305-764, Republic of Korea

ARTICLE INFO

Article history:
Received 14 April 2017
Received in revised form
10 November 2017
Accepted 12 November 2017
Available online 14 November 2017

Keywords:
MoS_2
Metal chalcogenides
Photoelectrocatalysis
Photoanode

ABSTRACT

Vertically aligned MoS_2 flakes were grown on indium tin oxide (ITO) and ITO/ZnO substrates using metalorganic chemical vapor deposition. The thickness of MoS_2 flakes was manipulated at the few-layer level (5–10), which is desirable for energy-storage and energy-conversion applications. For photoelectrochemical (PEC) cells, a few-layer flake photoelectrode yielded a considerably higher photocurrent density (930 $\mu A/cm^2$ at 0.2 V) than a MoS_2 thin-film photoelectrode (360 $\mu A/cm^2$ at 0.2 V) due to the former's high density of active sites, slow intraband relaxation rate from excitonic states, and low defect density. Furthermore, the heterostructure of ZnO/MoS_2 flakes exhibited a remarkably high photocurrent density of 1.6 mA/cm^2 at 0.2 V and a long-term stability under the PEC operating conditions because of its enhanced photogenerated carrier separation and transfer. Thus, such a heterostructure is promising as an efficient, nontoxic, inexpensive, and earth-abundant PEC electrode.

1. Introduction

Photoelectrochemical (PEC) splitting of water has been extensively studied as a promising approach to produce hydrogen gas for use as a clean non-fossil fuel [1]. Recently, metal chalcogenides, e.g., MoS_2, have attracted considerable attention as effective PEC catalysts because of their strong photoexcitation, good chemical stability, and earth abundance. MoS_2, which comprises a strong in-plane covalent bonding of S—Mo—S and weak out-of-plane van der Waals interaction between neighboring S—S layers, exhibits a relatively high mobility (a few hundred cm^2/Vs) and tunable bandgaps from ~1.2 eV for the indirect gap of the bulk form to ~1.9 eV for the direct gap of the monolayer [2–4]. Theoretical and experimental results indicate that the strong catalytic activity of MoS_2 arises from active S atom sites exposed along the edges. Yu et al. recently reported that the atoms in its basal plane may also be active [5]. The maximization of the density of such active sites in MoS_2 nanostructures is central to exploiting the full potential of this material for the hydrogen evolution reaction. Moreover, the manipulation of the thickness of MoS_2 structures is essential because it determines the bandgap and carrier transport properties of MoS_2 [2–6]. Velicky et al. revealed that few-layer (5–10) MoS_2 flakes provide a good compromise between large surface areas and sufficiently fast charge-carrier transport for energy storage and energy conversion applications [6].

Previously, few-layer MoS_2 flakes and nanosheets were synthesized using wet chemical approaches, such as chemical exfoliation and hydrothermal synthesis [7–9]. However, the desirable features of few-layer MoS_2 flakes are significantly deteriorated during the fabrication of thin-film-based PEC devices, which are usually prepared via spin coating or drop drying of a MoS_2 slurry. Integrated and stacked MoS_2 flakes, which interact through van der Waals forces, can essentially behave like bulk MoS_2. Chemical vapor deposition (CVD) has been demonstrated as a promising alternative approach for growing high-quality MoS_2 films with a scalable size and controllable thickness. However, most CVD studies have focused on flat MoS_2 sheets deposited on substrates via high-temperature growth (600 °C–1000 °C), which restricts the flexibility of the substrates [10,11]. Furthermore, the PEC performance of these flat MoS_2 films is significantly limited by their small specific surface area. Yin et al. coated exfoliated MoS_2 on a fluorine-doped tin oxide substrate for PEC electrodes and achieved a photocurrent density of 100 $\mu A/cm^2$ at 0.8 V; the photocurrent density reached 790 $\mu A/cm^2$ at 0.8 V after Au nanoparticles were loaded onto the MoS_2 electrodes [12]. Tang et al. fabricated the photoanode of TiO_2/MoS_2 by a two-step hydrothermal method, in which the electrode displayed noticeably enhanced photocurrent density of 1.2 mA/cm^2

---

* Corresponding author.
E-mail address: etkim@cnu.ac.kr (E.-T. Kim).

https://doi.org/10.1016/j.electacta.2017.11.089

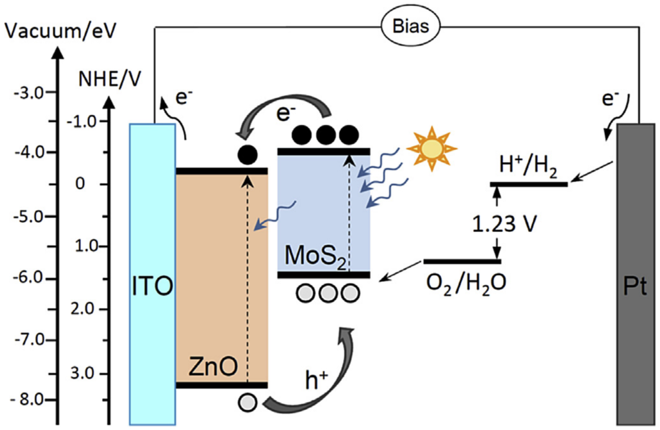

Fig. 1. Schematic of the charge generation and charge transfer processes in the ZnO/MoS_2 PEC cell under irradiation by simulated sunlight.

at 1.2 V, which was over two times higher than that of the pure TiO_2 electrode [13].

The design of heterostructures is another important factor that can be leveraged to improve PEC efficiency. Various heterostructures such as those of MoS_2/CdS, MoS_2/g-C_3N_4, MoS_2/ZnO nanoparticles, and MoS_2/TiO_2 nanoparticles have been extensively studied to enhance the separation and subsequent transfer of photogenerated electron–hole pairs using a built-in potential generated by an appropriate heterojunction [14–17]. To effectively transfer photogenerated electrons and holes to the proper electrodes, *n*-type semiconductors such as ZnO, TiO_2, and CdS should have proper contact with the counter electrode (e.g., Pt), as shown in Fig. 1. However, majority of previous PEC studies on such heterostructures considered MoS_2 films, which are less interesting because they have a small specific surface area [15]. On the other hand, MoS_2 flakes or nanosheets have been hybridized using electronically isolated TiO_2 or ZnO nanoparticles, which significantly reduce the potential for completely exploiting these heterostructures [16,17].

In this study, we observed enhanced PEC activity in a desirable heterostructure of few-layer MoS_2 flakes grown on an *n*-type ZnO layer. The MoS_2 flakes were vertically aligned to maximize their specific surface area and obtain a high density of active edges. By manipulating the gas-flow-rate ratio of precursors for the metal-organic CVD (MOCVD) reaction, the morphology of MoS_2 was tuned from a multilayer film to few-layer flakes.

2. Experimental methods

MoS_2 was synthesized at 250 °C under a pressure of 1 Torr for 5 min using an MOCVD system with $Mo(CO)_6$ and H_2S gas (5 vol% in balance N_2) as Mo and S precursors, respectively. $Mo(CO)_6$ was vaporized at 20 °C and delivered into a quartz tube using Ar gas. The total flow rate of the gases was fixed at 100 SCCM (standard cubic centimeter per minute), where the flow-rate ratio of the Ar carrier and H_2S gases varied with the corresponding ratios of 75:25, 50:50, and 25:75. Sample morphology was characterized via scanning electron microscopy (SEM, Hitachi S-4800) and transmission electron microscopy (TEM, Tecnai G^2 F30 S-Twin). The chemical states and composition of samples were characterized using X-ray

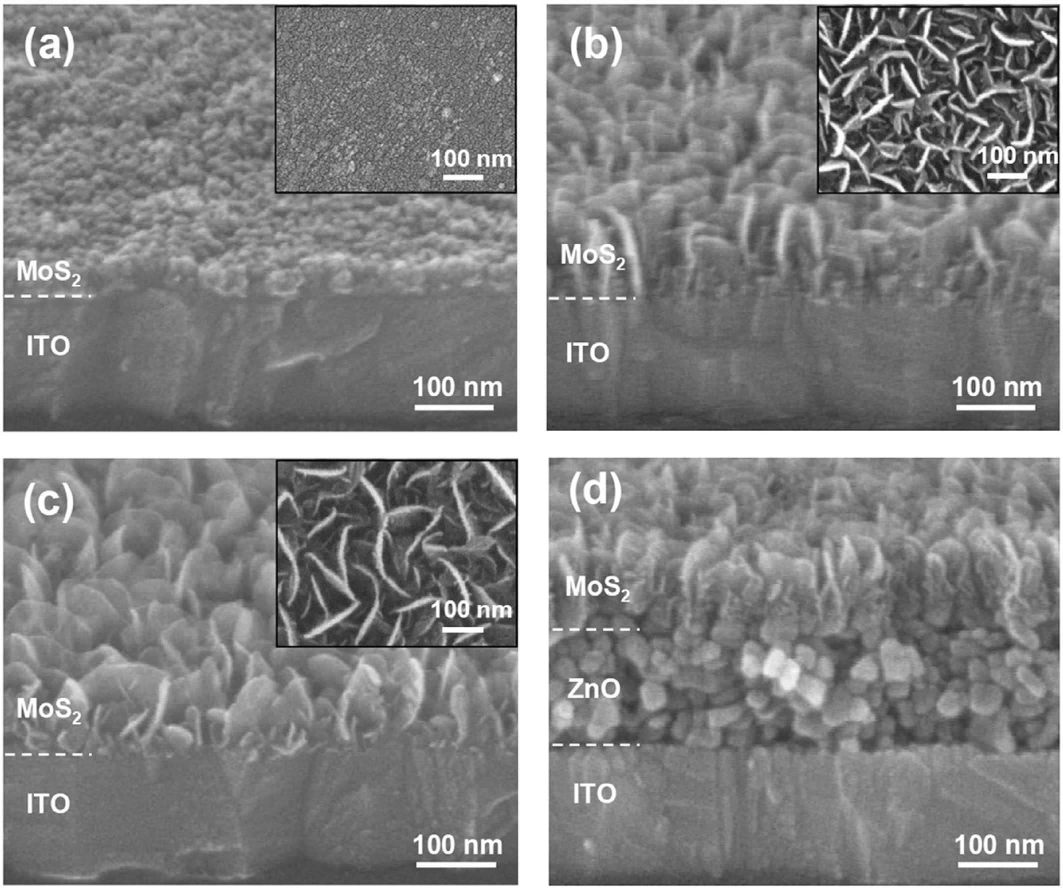

Fig. 2. SEM images of (a) sample S1, (b) sample S2, (c) sample S3, and (d) ZnO/MoS_2 flakes. The insets show the corresponding top-view SEM images.

photoelectron spectroscopy (XPS, Thermo Scientific MultiLab 2000 spectrometer). The structural properties of MoS_2 were investigated via micro-Raman spectroscopy using an excitation of 532 nm and a charge-coupled device detector. The sample optical properties were characterized via photoluminescence (PL) spectroscopy (excitation at 532 nm) and an ultraviolet–visible (UV–Vis) spectrophotometer (S-3100, SCINCO).

PEC cells were fabricated on 0.6×2 cm^2 indium tin oxide (ITO) glass substrates. ZnO/MoS_2 photoelectrodes were prepared by spin coating a ZnO nanoparticle suspension (5 wt% in ethanol, 50–100 nm average diameter) on an ITO substrate at 3000 rpm. Subsequently, MoS_2 was grown on the ZnO nanoparticle sample and counterpart sample, i.e., bare ITO glass, which were positioned adjacently. The working area of the PEC cells was fixed at 0.5×0.5 cm^2 using nonconductive epoxy to cover undesirable areas. PEC characterization was performed using a three-electrode system and an electrochemical analyzer (potentiostat/galvanostat 263 A). A Pt plate and KCl-saturated calomel (Hg/Hg_2Cl_2) were used as counter and reference electrodes, respectively. The electrolyte solution comprised 0.1 M Na_2S buffered with H_2SO_4. The light source comprised a 150 W Xe arc lamp delivering an intensity of 100 mW/cm^2 of simulated AM 1.5G irradiation. The current–voltage characteristics were recorded using a sourcemeter (Keithley 2400). Electrochemical impedance spectroscopy (EIS) of the electrodes was performed under constant light illumination (100 $mWcmm^{-2}$) at a bias of 0.2 V while varying the ac frequency in the range from 100 kHz to 100 mHz.

3. Results and discussion

The morphology of MoS_2 was significantly affected by the flow rate ratio of the Ar carrier gas to H_2S gas, which eventually determined the concentration ratio of the Mo^{4+} cation to S^{2-} anion in the CVD reaction (Fig. 2). A dense 60 nm-thick thin film with ~10–20 nm nanocrystallites was formed at a gas ratio of 75:25, hereinafter referred to as sample S1 (Fig. 2(a)). Upon decreasing the gas ratio to 50:50, the morphology of MoS_2 changed drastically to vertically aligned flakes, hereinafter referred to as sample S2 (Fig. 2(b)). The flakes were ~140 nm high, ~100 nm long, and densely packed on an ITO substrate. Upon decreasing the gas ratio to 25:75, the vertically aligned flakes developed further; consequently, the average flake length increased to ~200 nm, whereas the height did not change significantly (Fig. 2(c)). This sample is hereinafter referred to as sample S3. Similar densely packed vertically aligned flakes also formed on the ITO/ZnO nanoparticle substrates, as shown in Fig. 2(d). The size and shape of the MoS_2 flakes did not change significantly compared with those of the counterpart sample S3 grown on a bare ITO substrate. In general, the stoichiometric growth of compound semiconductors, e.g., MoS_2, occurs under anion-sufficient conditions because the sticking coefficient of metal cations is much higher than that of anions [18,19]. A S^{2-}-sufficient condition can facilitate layered growth of MoS_2 because chemisorbed Mo^{4+} cations are likely to properly bond two S^{2-} anions for layered MoS_2 (S–Mo–S). Upon increasing the ratio of Mo ions to S ions, impinged Mo elements were likely to immediately bond with the nearest Mo adatoms and result in

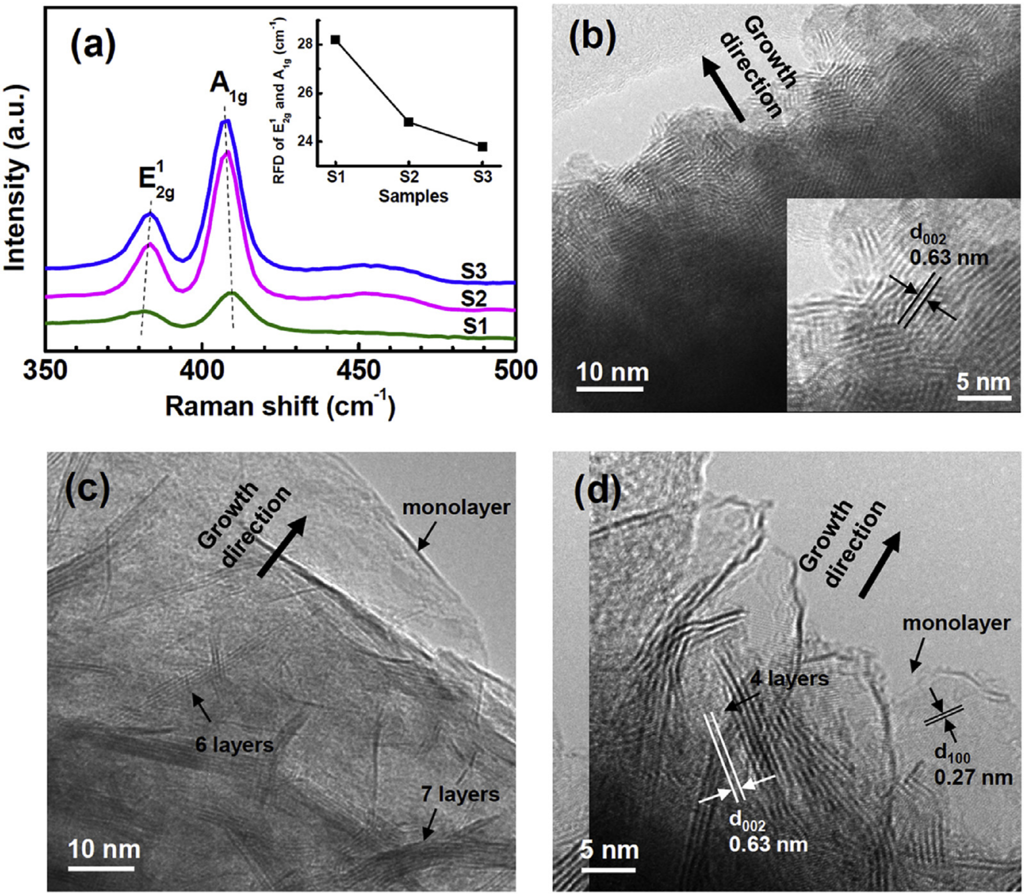

Fig. 3. (a) Raman spectra of samples S1, S2, and S3. The inset shows the RFD between the E^1_{2g} and A_{1g} Raman modes. (b) TEM image of sample S1. The inset shows a high-resolution TEM image. (c) Low-magnification and (d) high-resolution TEM images of sample S3.

particle growth rather than layer-by-layer growth [20,21].

To investigate the structural properties of MoS_2, Raman spectroscopy and TEM were applied. All the samples generated two strong Raman peaks that corresponded to the in-plane E^{1}_{2g} mode from the vibration of Mo and S atoms and the out-of-plane A_{1g} mode from the vibration of S atoms [2,22], as shown in Fig. 3(a). The E^{1}_{2g} and A_{1g} modes in sample S1 exhibited Raman peak positions at 381.6 and 409.8 cm^{-1}, respectively, which were almost the same as those observed for multilayer or bulk-like MoS_2 [3]. The E^{1}_{2g} and A_{1g} modes of sample S2 were blue shifted to 383.0 cm^{-1} and red shifted to 407.8 cm^{-1} with respect to those of sample S1, respectively. Sample S3 exhibited a slightly more-blue-shifted E^{1}_{2g} peak (383.5 cm^{-1}) and red-shifted A_{1g} peak (407.4 cm^{-1}). It has been reported that from the bulk to monolayer, the E^{1}_{2g} peak blue shifted, whereas the A_{1g} peak red shifted [3,23]. With a decreasing number of layers, the long-range Coulomb interlayer interaction weakened and resulted in high frequency of the in-plane E^{1}_{2g} mode. Meanwhile, the out-of-plane A_{1g} vibration appeared at a low frequency because of the diminished restoring force of the interlayer S—S atoms. The number of MoS_2 layers can be estimated from the relative frequency difference (RFD) between the E^{1}_{2g} and A_{1g} peaks [24,25]. As shown in the inset of Fig. 3(a), the RFD in sample S1 was 28.2 cm^{-1}, corresponding to the multilayers of MoS_2. The RFDs significantly decreased to 24.8 and 23.9 cm^{-1} for samples S2 and S3, respectively. The RFD of 23.9 cm^{-1} was estimated to correspond to three layers of MoS_2 [2]. These estimates were consistent with the results of TEM analyses. Sample S1 exhibited a typical polycrystalline microstructure with nanocrystallites of ~10—20 nm (Fig. 3(b)). By contrast, the flakes of sample S3 clearly contained a 2D layer structure that was 200 nm long and 140 nm high, as shown in Fig. 3(c). The interlayer spacing of 0.63 nm was consistent with that observed for MoS_2 [26]. The number of layers varied from a monolayer at the tip to a few layers (5—10) in the middle, as shown in Fig. 3(c) and (d). The flakes yielded a significant number of exposed layer edges, which acted as effective catalytic sites, due to the overlapping of such layers [27,28].

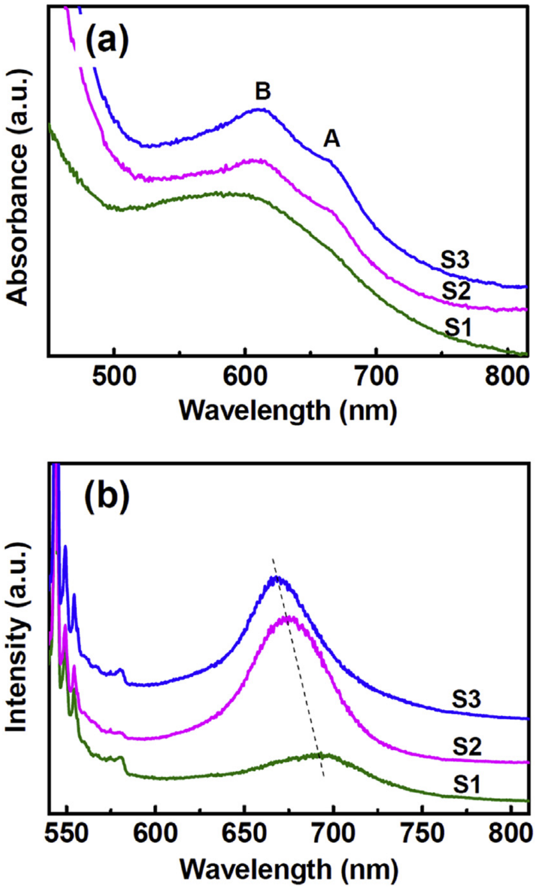

Fig. 4. (a) Absorption and (b) photoluminescence spectra of samples S1, S2, and S3.

We investigated the electronic structure of MoS_2 using UV—Vis absorption and PL spectroscopies. The vertically aligned samples of MoS_2 flakes (samples S2 and S3) exhibited two prominent absorption peaks at approximately 665 and 610 nm, whereas the MoS_2 thin film (sample S1) exhibited a broad peak between 600 and 700 nm (Fig. 4(a)). The two resonances, known as excitons A and B, respectively, were attributed to the direct excitonic transitions at the *K* point of the Brillouin zone [27]. Samples S2 and S3 presented strong PL peaks at 668 and 675 nm, respectively, as shown in Fig. 4(b). By contrast, sample S1 demonstrated a considerably weak PL peak at 692 nm. The PL peaks were consistent with the energy of exciton A, indicating that they originated from the direct bandgap transitions at the *K* point [29]. The most-blue shifted PL peak of sample S3 indicated the thinnest MoS_2 layer among the three samples. A decrease in the MoS_2 film thickness resulted in a slight blue shift in the PL peak [27]. Moreover, the vertically aligned flake samples exhibited a much higher PL efficiency than the thin-film sample. This significantly enhanced PL was attributed to a slow intraband relaxation rate from the excitonic states and a low defect density [29]. The former could be explained by an increased indirect bandgap energy of the few-layer MoS_2, and the latter was due to the layered MoS_2 structure, which was confirmed by TEM. The defects of the unsaturated Mo or S bonds introduced midgap states that acted as nonradiative-recombination sites for excitons [30]. The concentration of such defects could be significantly reduced in the S—Mo—S layered structure, which was grown under S^{2-} anion-sufficient conditions. The low defect density and slow intraband transition rate of the few-layer MoS_2 were beneficial for efficient transfer of electrons and holes onto the catalytic surface.

To evaluate the activity of the MoS_2 samples for PEC cells, we recorded linear-sweep voltammograms in the dark and under illumination. As shown in Fig. 5(a), sample S1 exhibited a photocurrent density of 360 $\mu A/cm^2$ at an applied potential of 0.2 V, whereas an ITO reference electrode yielded negligible photocurrent under illumination. By contrast, sample S3 showed a significantly increased photocurrent density of 930 $\mu A/cm^2$ at 0.2 V. This enhanced PEC activity was attributed to its unique vertically aligned few-layer structure. As discussed above, few-layer flakes not only produce a significant amount of catalytically active edge sites but are also beneficial for the efficient transfer of charge carriers to the catalytic surface. Moreover, the densely packed vertical flake structure inherently increased the specific interfacial area of the MoS_2/electrolyte. Meanwhile, samples S1 and S3 yielded nearly the same dark current-potential behavior from −1.0 V to −0.3 V (Fig. 5(b)). The dark current increases slowly and reaches approximately 100 $\mu A/cm^2$ at −0.3 V as the potential increased. As the potential further increased, the dark current of sample S1 plateaued to 0.2 V and then increased rapidly. By contrast, the dark current of sample S3 continuously increased. The dark current was attributed to the electrocatalysis and electrocorrosion of MoS_2, in which active S atoms can react with redox species in a solution [31]. However, a rapid increase above 0.2 V was mainly due to the electrocorrosion of MoS_2. Thus, the second peak also appeared in the photocurrent—potential curves above 0.2 V (Fig. 5(a)). After PEC measurement of sample 3 for 500 s, the MoS_2 flakes demonstrated to a slightly reduced height and dull flake tips, thereby indicating decomposition at their tips (see Supporting Information, Fig. S1). As

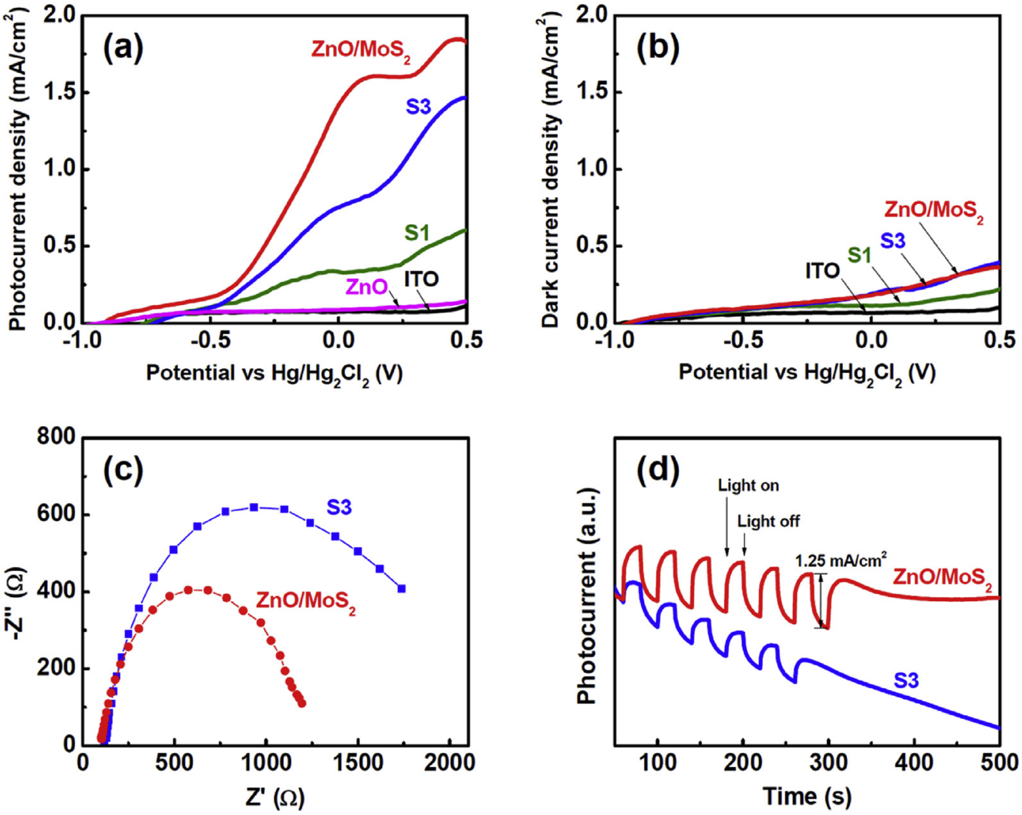

Fig. 5. (a) Photocurrent density–potential curves and (b) dark current density–potential curves of PEC cells with various working electrodes (ITO, ZnO, sample S1, sample S3, and ZnO/MoS_2 flakes). (c) Nyquist plots of sample S3 and ZnO/MoS_2 flakes. (d) Photocurrent versus time for sample S3 and ZnO/MoS_2 flakes as the working electrode at an applied potential of 0.2 V.

shown in Fig. 6, the XPS study confirmed that the composition of the MoS_2 surface also slightly changed after PEC measurement. The S composition was reduced from 57.4 at.% to 48.3 at.%, whereas the Mo composition was not significantly changed from 24.3 at.% to 23.7 at.%. The loss of S elements was attributed to the dissolution of active S atoms at the tip of the MoS_2 flakes.

To further enhance PEC activity, we used the heterostructure of ZnO/MoS_2 flakes. ZnO, as an *n*-type semiconductor, was chosen because of its wide direct bandgap (~3.37 eV), appropriate electron affinity (4.35 eV), excellent optical characteristics, and good chemical stability [32,33]. Considering the bandgap energy (~1.86 eV) and electron affinity (~4 eV) of the few-layer MoS_2 [34], ZnO/MoS_2 formed a staggered (type II) heterostructure with offset conduction and valence band edges of ~0.35 and ~1.86 eV, respectively (Fig. 1). The anodic photocurrent in Fig. 5(a) implies that MoS_2 was most likely an *n*-type semiconductor. As a result, the photogenerated electron–hole pairs of MoS_2 were expected to effectively separate and subsequently transfer to the Pt electrode through ZnO and onto the MoS_2 surface, respectively. As shown in Fig. 5(c), the Nyquist plots of EIS showed a small EIS semicircle for the heterostructure of ZnO/MoS_2 flakes, thereby indicating a decrease in charge transfer resistance and a suppression of charge recombination [35]. The photocurrent density of the heterostructure of ZnO/MoS_2 flakes increased remarkably to 1.6 mA/cm^2 at 0.2 V (Fig. 5(a)), whereas its dark current was nearly the same as that of sample S3 (Fig. 5(b)). Meanwhile, the open-circuit voltage (V_{oc}) of the heterostructure of ZnO/MoS_2 flakes (−0.92 V) presented a cathodic shift with respect to that (−0.72 V) of sample S3. Photocurrent production was minimal until it reached the water oxidation onset potential (e.g., −0.42 V for ZnO/MoS_2), which is generally defined by the potential at the intersection of the dark current and the tangent at the maximum slope of photocurrent [36]. The small photocurrent increase from −0.92 V to −0.42 V was partially due to oxidation of S^{2-} ions by photogenerated holes, whereas the significant photocurrent gain above −0.42 V was attributed to water oxidation. Gas bubbles generated from the photoanode (MoS_2) and dark cathode (Pt) during PEC measurement (see Supporting Information, Fig. S2). To further quantify PEC performance, the photoconversion efficiencies (η) were estimated through the following equation [37]:

$$\eta = J(E^{o} - V_{app})/P_{light},$$

Where *J* is the photocurrent density (mA/cm^2) at the applied potential, E^o is the standard reversible potential (1.23 V), V_{app} is applied potential, and P_{light} is the power density of illumination. As the potential increased, the photoconversion efficiency of the heterostructure of ZnO/MoS_2 flakes continuously increased and reached a maximum value of 0.6% at 0 V (see Supporting Information, Fig. S2 and Table S1). The maximum values of the photoconversion efficiency of samples S1 and S3 were 0.18% and 0.4%, respectively. The photoconversion efficiency and saturated photocurrent density of the heterostructure of ZnO/MoS_2 flakes were at least comparable with various photoanodes reported recently, such as exfoliated MoS_2, MoS_2 nanosheets/TiO_2 nanoparticles, and CoO_x/TiO_2–TaON [12,13,38,39]. Moreover, the

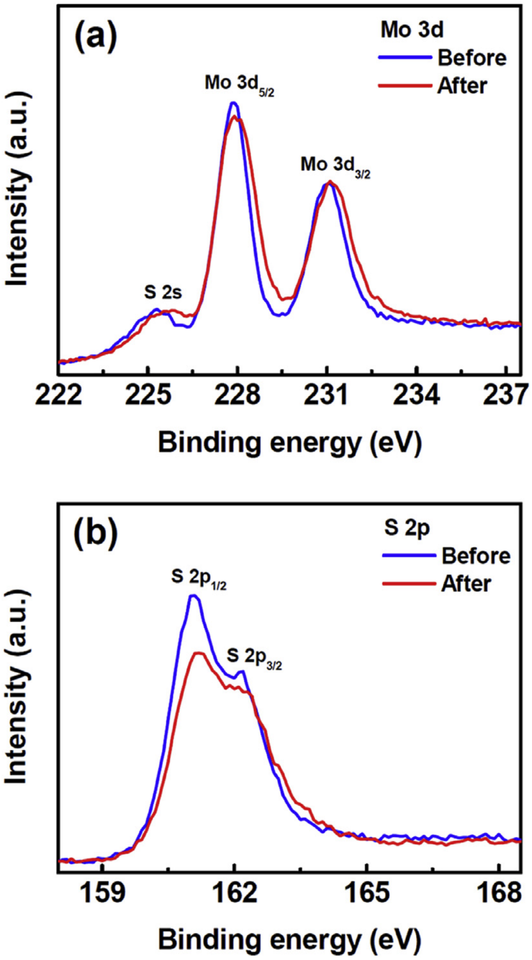

Fig. 6. XPS spectra of sample 3 before and after PEC measurement: (a) Mo 3 d and (b) S 2p core levels.

photocurrent of the heterostructure of ZnO/MoS_2 flakes did not change significantly through 500 s illumination, whereas the photocurrent of sample S3 decreased continuously (Fig. 5(d)). The photocurrent of the heterostructure of ZnO/MoS_2 flakes decayed initially but saturated shortly above 400 s. The decayed photocurrent was attributed to the recombination of the photogenerated holes with electrons [40]. The photocurrent became stable as the transfer and generation of photogenerated electron–hole pairs reached equilibration. Thus, the stable photocurrent suggested effective separation and transfer of the photogenerated electron–hole pairs in the heterojunction of ZnO/MoS_2 flakes.

To observe the effect of the thickness of the MoS_2 flake layer on PEC performance, a thin MoS_2 flake layer was prepared on the ITO/ZnO substrates. The thickness of the MoS_2 flake layer was manipulated at approximately 90 nm for 3.5 min of growth time (Fig. 7(a)). Dark and photo currents decreased with the thickness of the MoS_2 flake layer (Fig. 7(b)). Thus, the photo-to-dark current density ratios were not significantly changed for the ZnO/140 nm-thick MoS_2 and the ZnO/90 nm-thick MoS_2 heterostructures (6.4 and 6.8 at 0.2 V, respectively). However, the differences between the photo and dark current densities of the ZnO/140 nm-thick MoS_2 (1350 $\mu A/cm^2$ at 0.2 V) were larger than those of ZnO/90 nm-thick MoS_2 (1150 $\mu A/cm^2$ at 0.2 V), thereby suggesting that long MoS_2 flakes were advantageous in obtaining hydrogen gas through the PEC reaction.

4. Conclusions

Vertically aligned few-layer MoS_2 flakes were grown on ITO and ITO/ZnO substrates using MOCVD. The few-layer flakes were synthesized using enhanced S–Mo–S layered growth under S^{2-} sufficient growth conditions, whereas a nanocrystalline film formed at a high flow rate ratio of Mo to S precursors (75:25). The few-layer flakes not only possessed a high specific density and a high density of active edges but also exhibited a strong PL peak via direct excitonic transitions at the Brillouin-zone K point (668 nm), indicating a slow intraband relaxation rate from the excitonic states and a low defect density. As a result, the few-layer flake electrode exhibited a considerably higher photocurrent density (930 $\mu A/cm^2$ at 0.2 V) than the thin-film electrode (360 $\mu A/cm^2$ at 0.2 V) for PEC cells. Moreover, the PEC performance and long-term stability remarkably improved when the heterostructure of ZnO/MoS_2 flakes was used because of its enhanced photogenerated electron–hole separation and transfer properties. The results indicate that ZnO/MoS_2 flakes are promising candidates as nontoxic, inexpensive, and earth-abundant photoelectrodes for an efficient hydrogen evolution reaction.

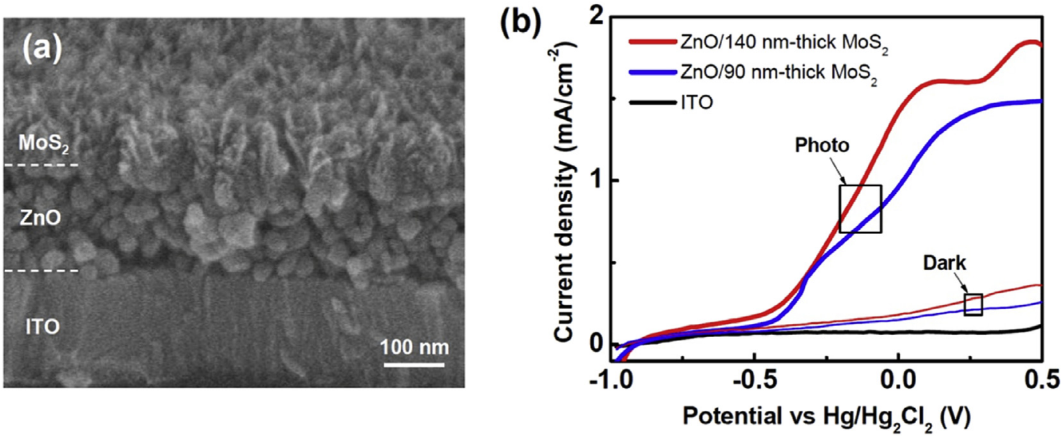

Fig. 7. (a) Cross-sectional SEM image of ZnO/90 nm-thick MoS_2 flakes. (b) Photocurrent density– and dark current density–potential curves of PEC cells with ZnO/140 nm-thick MoS_2 and ZnO/90 nm-thick MoS_2 heterostructures as working electrodes.

Acknowledgements

This study was supported by Basic Research Program through the National Research Foundation of Korea (NRF) funded by the Ministry of Education (NRF-2015R1D1A1A01059069).

Appendix A. Supplementary data

Supplementary data related to this article can be found at https://doi.org/10.1016/j.electacta.2017.11.089.

References

[1] M.G. Walter, E.L. Warren, J.R. McKone, S.W. Boettcher, Q. Mi, E.A. Santori, N.S. Lewis, Solar water splitting cells, Chem. Rev. 110 (2010) 6446.

[2] C. Lee, H. Yan, L.E. Brus, T.F. Heinz, J. Hone, S. Ryu, Anomalous lattice vibrations of single- and few-layer MoS$_2$, ACS Nano 4 (2010) 2695.

[3] H. Li, Q. Zhang, C.C.R. Yap, B.K. Tay, T.H.T. Edwin, A. Olivier, D. Baillargeat, From bulk to monolayer MoS$_2$: evolution of raman scattering, Adv. Funct. Mater 22 (2012) 1385.

[4] K.F. Mak, C. Lee, J. Hone, J. Shan, T.F. Heinz, Atomically thin MoS$_2$: a new direct-gap semiconductor, Phys. Rev. Lett. 105 (2010) 136805.

[5] Y. Yu, S.-Y. Huang, Y. Li, S.N. Steinmann, W. Yang, L. Cao, Layer-dependent electrocatalysis of MoS$_2$ for hydrogen evolution, Nano Lett. 14 (2014) 553.

[6] M. Velický, M.A. Bissett, C.R. Woods, P.S. Toth, T. Georgiou, I.A. Kinloch, K.S. Novoselov, R.A.W. Dryfe, Photoelectrochemistry of pristine mono- and few-layer MoS$_2$, Nano Lett. 16 (2016) 2023.

[7] S. Ji, Z. Yang, C. Zhang, Z. Liu, W.W. Tjiu, I.Y. Phang, Z. Zhang, J. Pan, T. Liu, Exfoliated MoS$_2$ nanosheets as efficient catalysts for electrochemical hydrogen evolution, Electrochim. Acta 109 (2013) 269.

[8] J. Deng, W. Yuan, P. Ren, Y. Wang, D. Deng, Z. Zhang, X. Bao, High-performance hydrogen evolution electrocatalysis by layer-controlled MoS$_2$ nanosheets, RSC Adv. 4 (2014) 34733.

[9] X. Dai, Z. Li, K. Du, H. Sun, Y. Yang, X. Zhang, X. Ma, J. Wang, Facile synthesis of in−situ nitrogenated graphene decorated by few−layer MoS$_2$ for hydrogen evolution reaction, Electrochim. Acta 171 (2015) 72.

[10] A. Gupta, T. Sakthivel, S. Seal, Recent development in 2D materials beyond graphene, Prog. Mater. Sci. 73 (2015) 44.

[11] G. Zhang, H. Liu, J. Qu, J. Li, Two-dimensional layered MoS$_2$: rational design, properties and electrochemical applications, Energy Environ. Sci. 9 (2016) 1190.

[12] Z. Yin, B. Chen, M. Bosman, X. Cao, J. Chen, B. Zheng, H. Zhang, Au nanoparticle-modified MoS$_2$ nanosheet-based photoelectrochemical cells for water splitting, Small 10 (2014) 3537.

[13] R. Tang, R. Yin, S. Zhou, T. Ge, Z. Yuan, L. Zhang, L. Yin, Layered MoS$_2$ coupled MOFs-derived dual-phase TiO$_2$ for enhanced photoelectrochemical performance, J. Mater. Chem. A 5 (2017) 4962.

[14] Y. Liu, Y.-X. Yu, W.-D. Zhang, MoS2/CdS heterojunction with high photoelectrochemical activity for H2 evolution under visible light: the role of MoS$_2$, J. Phys. Chem. C 117 (2013) 12949.

[15] L. Ye, D. Wang, S. Chen, Fabrication and enhanced photoelectrochemical performance of MoS$_2$/S-doped g-C3N4 heterojunction film, ACS Appl. Mater. Interfaces 8 (2016) 5280.

[16] Y.-H. Tan, K. Yu, J.-Z. Li, H. Fu, Z.-Q. Zhu, MoS$_2$@ZnO nano-heterojunctions with enhanced photocatalysis and field emission properties, J. Appl. Phys. 116 (2014) 064305.

[17] R. Xiaohui, Q. Xiang, S. Yongzhen, X. Si, X. Guanghua, Z. Zhen, H. Zongyu, Z. Jianxin, 2D co-catalytic MoS$_2$ nanosheets embedded with 1D TiO$_2$ nanoparticles for enhancing photocatalytic activity, J. Phys. D. Appl. Phys. 49 (2016), 315304.

[18] J.R. Arthur, Surface stoichiometry and structure of GaAs, Surf. Sci. 43 (1974) 449.

[19] C.T. Foxon, B.A. Joyce, Interaction kinetics of As$_2$ and Ga on (100) GaAs surfaces, Surf. Sci. 64 (1977) 293.

[20] K. Kang, S. Xie, L. Huang, Y. Han, P.Y. Huang, K.F. Mak, C.-J. Kim, D. Muller, J. Park, High-mobility three-atom-thick semiconducting films with wafer-scale homogeneity, Nature 520 (2015) 656.

[21] Y.-H. Lee, X.-Q. Zhang, W. Zhang, M.-T. Chang, C.-T. Lin, K.-D. Chang, Y.-C. Yu, J.T.-W. Wang, C.-S. Chang, L.-J. Li, T.-W. Lin, Synthesis of large-area MoS$_2$ atomic layers with chemical vapor deposition, Adv. Mater 24 (2012) 2320.

[22] Z. Lin, M.T. Thee, A.L. Elías, S. Feng, C. Zhou, K. Fujisawa, N. Perea-López, V. Carozo, H. Terrones, M. Terrones, Facile synthesis of MoS$_2$ and Mo$_x$W$_{1-x}$S$_2$ triangular monolayers, Apl. Mater 2 (2014), 092514.

[23] M. Ye, D. Winslow, D. Zhang, R. Pandey, Y. Yap, Recent advancement on the optical properties of two-dimensional molybdenum disulfide (MoS$_2$) thin films, Photonics 2 (2015) 288.

[24] J. Jeon, S.K. Jang, S.M. Jeon, G. Yoo, Y.H. Jang, J.-H. Park, S. Lee, Layer-controlled CVD growth of large-area two-dimensional MoS$_2$ films, Nanoscale 7 (2015) 1688.

[25] C. Yim, M. O'Brien, N. McEvoy, S. Winters, I. Mirza, J.G. Lunney, G.S. Duesberg, Investigation of the optical properties of MoS$_2$ thin films using spectroscopic ellipsometry, Appl. Phys. Lett. 104 (2014) 103114.

[26] F. Carraro, L. Calvillo, M. Cattelan, M. Favaro, M. Righetto, S. Nappini, I. Píš, V. Celorrio, D.J. Fermín, A. Martucci, S. Agnoli, G. Granozzi, Fast one-pot synthesis of MoS$_2$/crumpled graphene p−n nanonjunctions for enhanced photoelectrochemical hydrogen production, ACS Appl. Mater. Interfaces 7 (2015) 25685.

[27] G. Eda, H. Yamaguchi, D. Voiry, T. Fujita, M. Chen, M. Chhowalla, Photoluminescence from chemically exfoliated MoS$_2$, Nano Lett. 11 (2011) 5111.

[28] T.F. Jaramillo, K.P. Jørgensen, J. Bonde, J.H. Nielsen, S. Horch, I. Chorkendorff, Identification of active edge sites for electrochemical H$_2$ Evolution from MoS$_2$ nanocatalysts, Science 317 (2007) 100.

[29] A. Splendiani, L. Sun, Y. Zhang, T. Li, J. Kim, C.-Y. Chim, G. Galli, F. Wang, Emerging photoluminescence in monolayer MoS$_2$, Nano Lett. 10 (2010) 1271.

[30] K.K. Kam, B.A. Parkinson, Detailed photocurrent spectroscopy of the semiconducting group VIB transition metal dichalcogenides, J. Phys. Chem. 86 (1982) 463.

[31] K. Chang, Z. Mei, T. Wang, Q. Kang, S. Ouyang, J. Ye, MoS$_2$/graphene cocatalyst for efficient photocatalytic H$_2$ evolution under visible light irradiation, ACS Nano 8 (2014) 7078.

[32] S. Hernández, V. Cauda, A. Chiodoni, S. Dallorto, A. Sacco, D. Hidalgo, E. Celasco, C.F. Pirri, Optimization of 1D ZnO@TiO2 core−shell nanostructures for enhanced photoelectrochemical water splitting under solar light illumination, ACS Appl. Mater. Interfaces 6 (2014) 12153.

[33] Y. Sun, J.H. Seo, C.J. Takacs, J. Seifter, A.J. Heeger, Inverted polymer solar cells integrated with a low-temperature-annealed sol-gel-derived ZnO film as an electron transport layer, Adv. Mater 23 (2011) 1679.

[34] H. Zhong, R. Quhe, Y. Wang, Z. Ni, M. Ye, Z. Song, Y. Pan, J. Yang, L. Yang, M. Lei, J. Shi, J. Lu, Interfacial properties of monolayer and bilayer MoS$_2$ contacts with metals: beyond the energy band calculations, Sci. Rep. 6 (2016) 21786.

[35] L.J. Hoyos, D.F. Rivera, A.F. Gualdrón-Reyes, R. Ospina, J. Rodríguez-Pereira, J.L. Ropero-Vega, M.E. Niño-Gómez, Influence of immersion cycles during n−β−Bi$_2$O$_3$ sensitization on the photoelectrochemical behaviour of N−F−codoped TiO$_2$ nanotubes, Appl. Surf. Sci. 423 (2017) 917.

[36] D. Cao, W. Luo, J. Feng, X. Zhao, Z. Li, Z. Zou, Cathodic shift of onset potential for water oxidation on a Ti4+ doped Fe2O3 photoanode by suppressing the back reaction, Energy Environ. Sci. 7 (2014) 752.

[37] S.U.M. Khan, M. Al-Shahry, W.B. Ingler Jr., Efficient photochemical water splitting by a chemically modified n-TiO$_2$, Science 297 (2002) 2243.

[38] X. Ren, X. Qi, Y. Shen, S. Xiao, G. Xu, Z. Zhang, Z. Huang, J. Zhong, 2D co-catalytic MoS$_2$ nanosheets embedded with 1D TiO$_2$nanoparticles for enhancing photocatalytic activity, J. Phys. D. Appl. Phys. 49 (2016), 315304.

[39] S.S. Gujral, A.N. Simonov, M. Higashi, X.Y. Fang, R. Abe, L. Spiccia, Highly dispersed cobalt oxide on TaON as efficient photoanodes for long-term solar water splitting, ACS Catal. 6 (2016) 3404.

[40] S.J.A. Moniz, S.A. Shevlin, D.J. Martin, Z.-X. Guo, J. Tang, Visible-light driven heterojunction photocatalysts for water splitting - a critical review, Energy Environ. Sci. 8 (2015) 731.